ACS MATERIALS LETTERS

www.acsmaterialsletters.org

LETTER

Microwave Heating of Nanocrystals for Rapid, Low-Aggregation Intermetallic Phase Transformations

Daniel J. Rosen, Alexandre C. Foucher, Jennifer D. Lee, Shengsong Yang, Emanuele Marino, Eric A. Stach, and Christopher B. Murray*

Cite This: *ACS Materials Lett.* 2022, 4, 823–830

Read Online

ACCESS | Metrics & More | Article Recommendations | Supporting Information

ABSTRACT: The use of intermetallic Pt–Co nanocrystals (NCs) for the electrocatalytic oxygen reduction reaction is quickly gaining interest thanks to the higher electrochemical stability of the intermetallic $L1_0$ phase compared to a random alloy A1 phase. However, the thermal treatment that enables the intermetallic phase transformation also causes considerable NC aggregation, resulting in a significant loss of electrochemically active surface area. Herein, we report the use of microwave radiation to induce the intermetallic phase transformation in Cu-doped Pt–Co NCs. We demonstrate that microwave radiation reduces NC aggregation while allowing for a complete phase transformation in only 30 s. These microwave-treated NCs demonstrate higher mass activity for the oxygen reduction reaction while maintaining electrochemical stability similar to the thermally annealed samples.

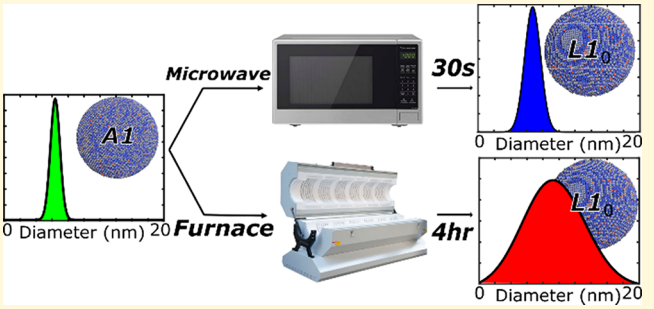

Intermetallic nanocrystals (NCs) are one of the most studied classes of materials for electrocatalysis[1−6] due to their high electrochemical stability[7−11] at lower precious metal loadings.[2,6,8,12−14] Pt–Co intermetallic face-centered-tetragonal (fct) phase ($L1_0$) NCs have been demonstrated as viable electrocatalysts for the oxygen reduction reaction (ORR).[7,13−18] The ability to perform the ORR with high electrochemical stability while decreasing the Pt loading is of key importance for proton exchange membrane fuel cells (PEMFCs),[10,14,19−21] with the capability of providing a source of clean energy able to compete with fossil fuels.[22] To make PEMFCs economically viable, there is a need to optimize the activity of the catalyst per unit Pt,[14,22] also known as the mass activity.

We use near-monodisperse Cu-doped $PtCo_2$ NCs in the intermetallic $L1_0$ phase as a model system. Copper-doping is known to reduce the barrier associated with the phase transformation.[9,23,24] The $L1_0$ phase is desirable because of simultaneously higher electrochemical stability and lower cobalt leaching during catalysis than the random alloy (A1) phase.[1−3,6−8,13,15,19,25] Typically, as-synthesized A1 face-centered-cubic (fcc) phase NCs are transformed into intermetallic $L1_0$ NCs by a thermal treatment that involves temperatures exceeding 400 °C over several hours.[1,2,6,13,26,27] During this process, NC aggregation, or sintering, occurs, leading to a decrease in the electrochemically active surface area (ECSA) and resulting in a decrease in mass activity for the ORR.[2,7,13,14]

Several literature reports have attempted to prevent NCs from aggregating during the thermal treatment by anchoring the NCs to the substrate,[11,20,21] or by synthesizing the NCs directly in the intermetallic phase.[14,15,28−32] Other methods have demonstrated a monodisperse dispersion of intermetallic NCs; however, these require a specialized technique such as Joule heating[33] or electrochemical dealloying.[30,34−36] So far, no method has shown a complete phase transformation with minimized aggregation.

Microwave heating is well-known as an efficient method to introduce large amounts of energy into materials. At the bulk scale, the use of microwaves to trigger phase transformations has been well studied.[37−40] At the nanoscale, microwaves have been used as a method of NC synthesis,[28,29,31,38] or catalytic excitation,[33,41,42] but they have not yet been used to induce intermetallic phase transformations. Microwave irradiation at the nanoscale allows localized heat generation from the NCs rather than their environment.[37−39] Localized heating allows for

Received: February 21, 2022
Accepted: March 25, 2022
Published: March 30, 2022

https://doi.org/10.1021/acsmaterialslett.2c00174
ACS Materials Lett. 2022, 4, 823–830

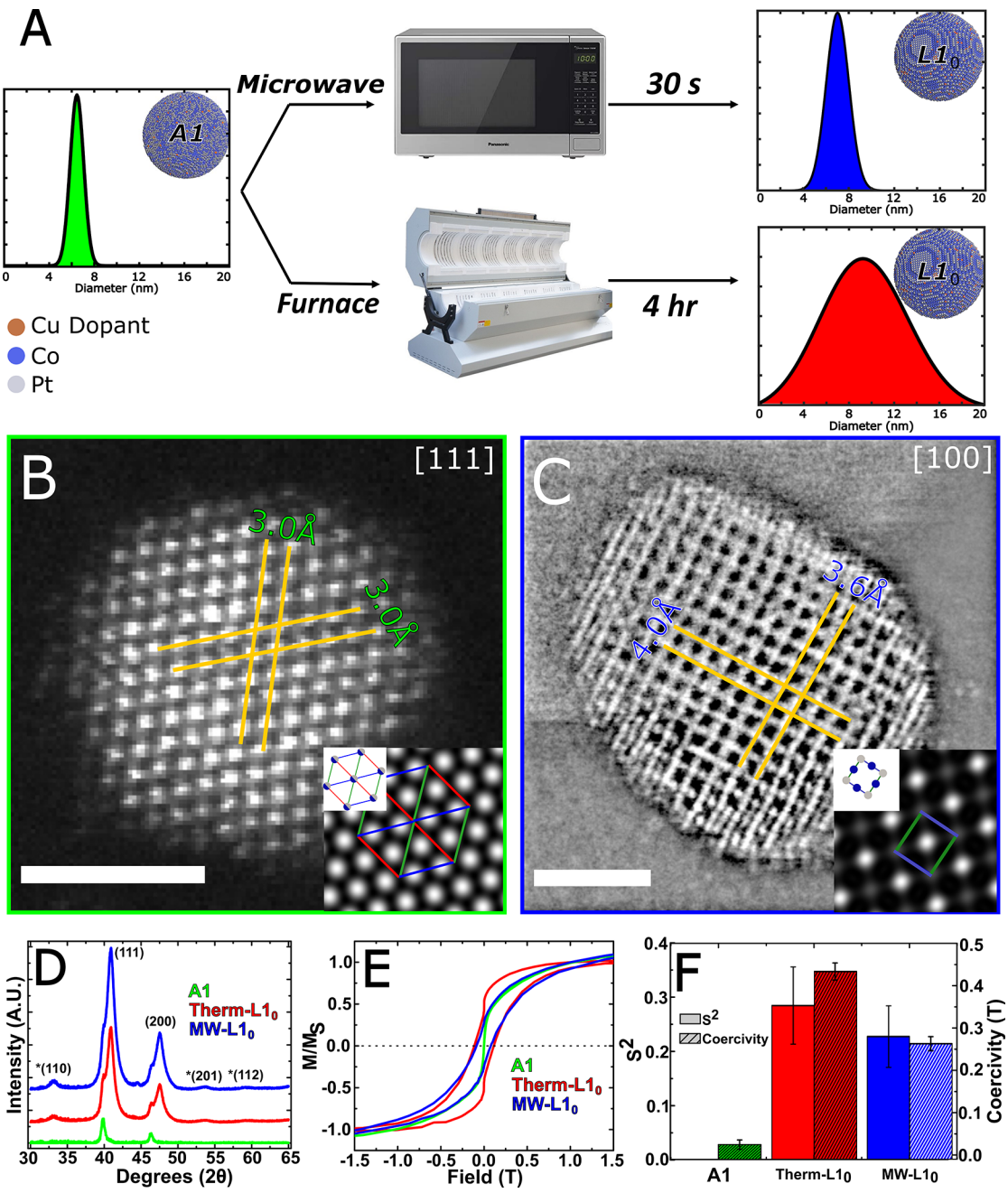

Figure 1. (A) Schematic representation of microwave- versus furnace-based transformation method including simulated 5 nm A1 and $L1_0$ NCs. Atomic-resolution dark field STEM micrographs are shown in panel (B) A1 and (C) MW-$L1_0$ NCs; insets show simulated HAADF-STEM lattice with corresponding unit cell. The approximate zone axis orientation is labeled in the upper right of each micrograph. A slight deviation from the exact zone axis orientation leads to small differences between the acquired micrograph and the inset simulation. (D) X-ray Diffraction patterns with "*" representing superlattice peaks associated with the $L1_0$ phase. (E) Magnetic hysteresis curves for A1, Therm-$L1_0$, and MW-$L1_0$ samples with a dotted line at magnetization equal to 0. (F) Degree of ordering and magnetic coercivity for the samples previously mentioned.

a temperature difference between the NCs and their local support environment of nearly 100 °C.[43,44]

In this work, we use localized microwave-induced NC heating to efficiently trigger a phase transformation from the A1 phase to the $L1_0$ phase of Cu-doped $PtCo_2$ NCs, 7.0 ± 1.0 nm in diameter. Using microwave heating minimizes aggregation and decreases the treatment time to just a few seconds, compared to several hours for thermally annealed samples. The shorter treatment beats material diffusion, decreasing NC aggregation and increasing their mass activity compared to thermally annealed NCs.

The methods used in this paper are described in detail in the Experimental Methods section.[13,45,46] Cu-doped Pt−Co NCs are synthesized in the A1 phase, as shown in Figure S1, by modifying previously reported recipes.[13,45] The NCs were deposited at 20 wt % onto Vulcan carbon and treated to remove any surface ligands. To induce a phase transformation from the A1 to the $L1_0$ phase, the A1 sample is divided equally into two aliquots subjected to either microwave radiation or conventional tube furnace thermal annealing. For the microwave treatment, we found that a commercial microwave represents a good option over laboratory-grade microwaves as they allow for tunable

https://doi.org/10.1021/acsmaterialslett.2c00174
ACS Materials Lett. 2022, 4, 823−830

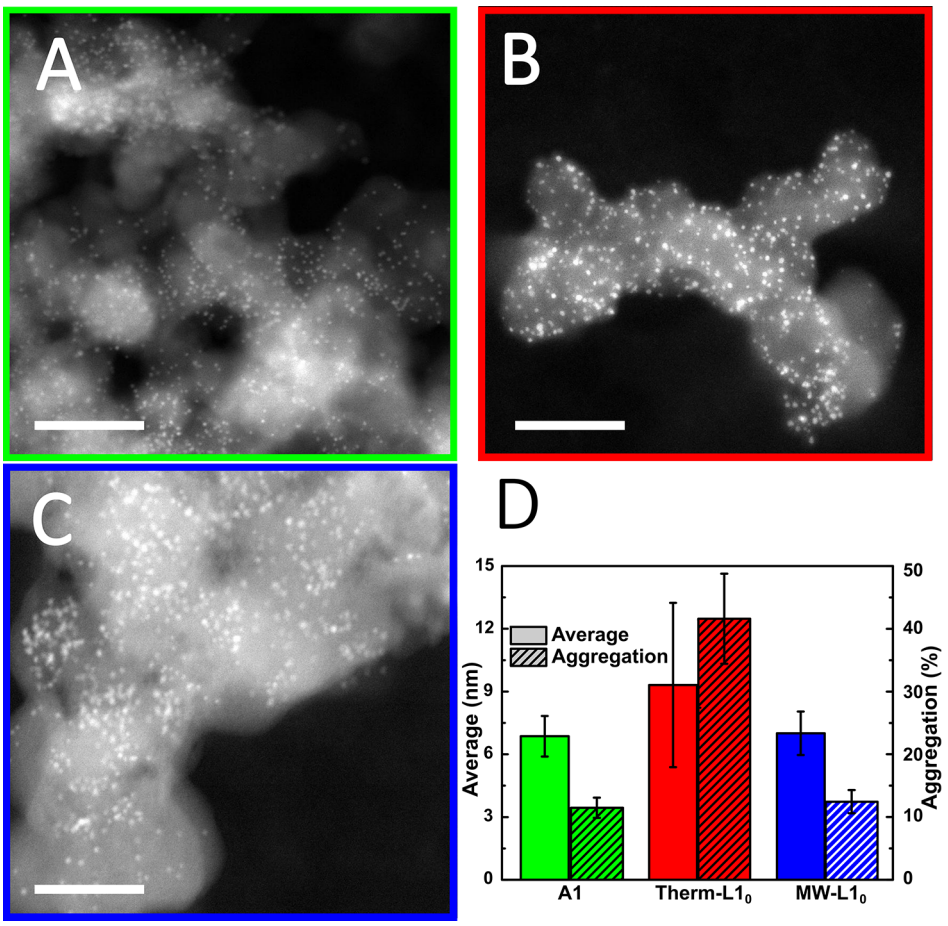

Figure 2. (A−C) STEM micrographs of A1 (green), Therm-L1$_0$ (red) Movie S1, and MW-L1$_0$ (blue) Movie S2 NCs, respectively. All scale bars in panels A−C are 100 nm. (D) Size distribution and the aggregation percentage for each sample. The error bars for the average represent the standard deviation, while the error bars for aggregation represent the error based on multiple sample transformations.

output power for a limited cost (comparison in section S2). However, an accurate determination of the microwave hotspot is crucial to ensure that the phase transformation occurs. We determine the microwave hotspot using a thermally sensitive grid as shown in Figures S2 and S3 and place the sample in the hotspot in a sealed quartz holder. The holder is then filled with 5% H_2 and 95% N_2, and the sample is treated for the desired time at an initial pressure of 1 atm (MW-L1$_0$). Instead, the thermally annealed samples are treated for 4 h at 650 °C in a tube furnace under 5% H_2 and 95% N_2 to drive the phase transformation (Therm-L1$_0$).[13] A schematic comparison of the processing of the NCs after both microwave and thermal treatments is shown in Figure 1A. Evidence of an intermetallic phase transformation is shown in Figure 1B−G.

Figure 1B−C shows atomic-resolution high-angle annular dark field-scanning transmission electron microscopy (HAADF-STEM) micrographs of A1 and MW-L1$_0$ NCs, respectively. The NC shown in Figure 1B shows no elemental contrast and is characterized by lattice spacings of 3.0 by 3.0 Å, identifying the A1 crystal phase. Instead, the NC shown in Figure 1C shows intermetallic patterning of Pt and Co atoms, resulting in a shift in lattice spacing to 4.0 by 3.6 Å that confirms a transformation into the L1$_0$ phase. We use X-ray diffraction (XRD) to show this transformation on an ensemble scale, as shown in Figure 1D. We compare the XRD spectra in Figure 1D to a simulated spectrum[47] of the same system, shown in Figure S7, to calculate the degree of ordering (S^2) of the NCs.[13] As described in detail in section S4, the expected value of the degree of ordering of fully transformed L1$_0$ NCs is $S^2 = 0.24$. Both thermal annealing and microwave heating result in values of $S^2 = 0.28 \pm 0.07$ and 0.22 ± 0.06, respectively, confirming that both treatments successfully transformed the NCs from the A1 phase to the L1$_0$ phase. This phase transformation affects the magnetic properties of the NCs, which we monitor by using AC magnetic hysteresis testing with a superconducting quantum interference design (SQUID), as shown in Figure 1E. Because the Pt−Co system is expected to transition from a superparamagnetic state in the A1 phase to a ferromagnetic state in the L1$_0$ phase,[7,13] we use the magnetic coercivity (H_c) as an indicator of phase transformation. We find that the A1 phase has a H_c of 0.025 ± 0.011 T, while the Therm-L1$_0$ and MW-L1$_0$ show increased H_c values of 0.433 ± 0.020 T and 0.263 ± 0.017 T, respectively. Interestingly, a close inspection of the magnetic hysteresis curve for Therm-L1$_0$ shown in Figure 1F reveals two kinks, narrowing the curve near the origin. We propose that this is due to the leaching and nucleation of Co during the thermal annealing, resulting in phase separation. Other reports have also shown that the thermal annealing of Pt−Co NCs can induce phase-separation.[13] Importantly, these kinks are not observed for the MW-L1$_0$ samples, likely due to the lower reaction time that characterizes the microwave treatment, suppressing the nucleation of Co. The XRD and SQUID characterization for all samples is summarized in Figure 1F.

https://doi.org/10.1021/acsmaterialslett.2c00174
ACS Materials Lett. 2022, 4, 823−830

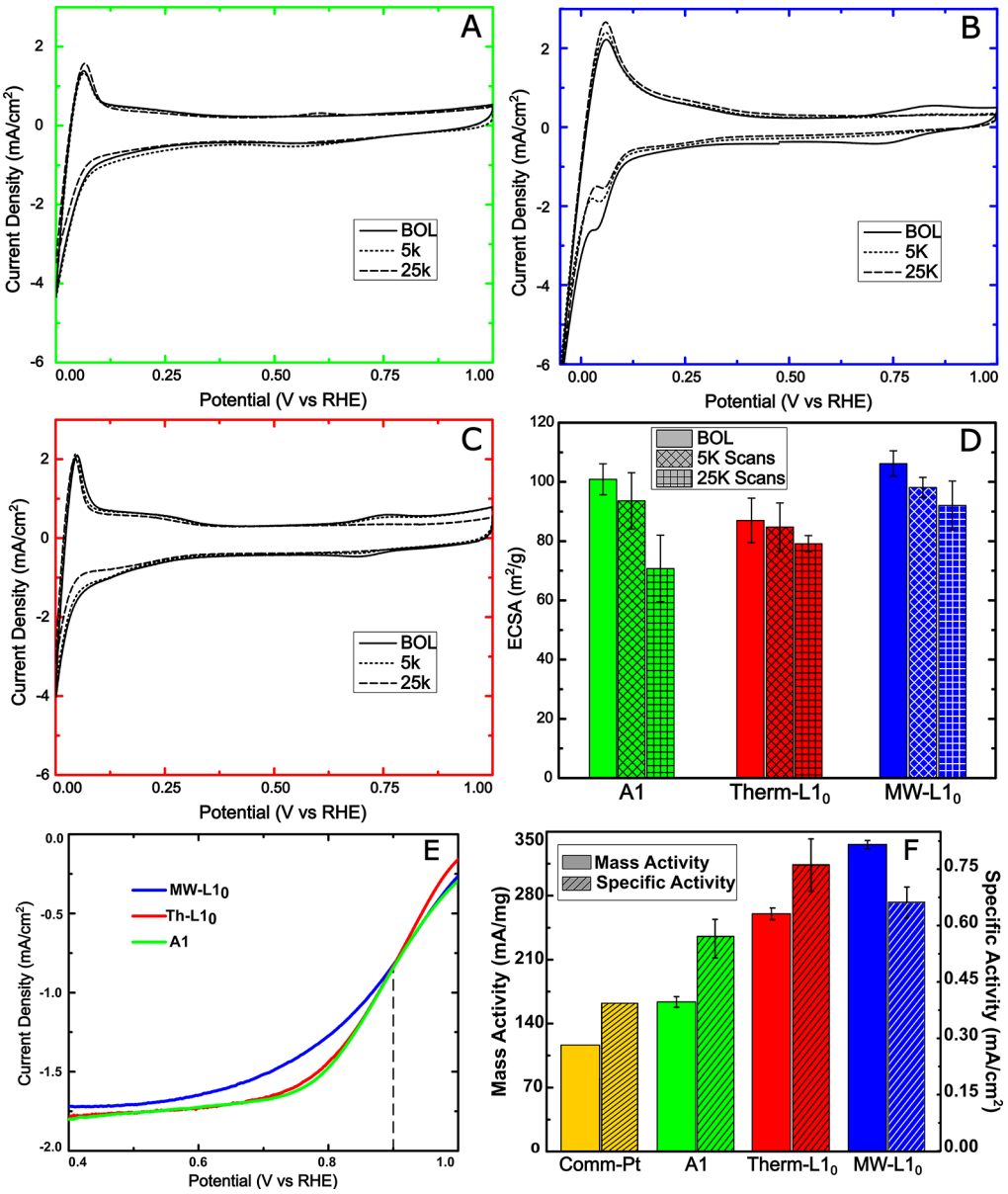

Figure 3. (A–C) Electrochemical stability data at the beginning of life, after 5000 and 25 000 catalytic cycles for $PtCo_2Cu_{0.19}$ in the A1 phase, Therm-$L1_0$, and MW-$L1_0$, respectively. (D) Summary of the electrochemical stability data. (E) ORR activity data with a drop-down line at 0.9 V vs RHE (F) Summary of the mass and specific activities for these samples and commercial Pt (Comm-Pt) as described in section S6.

To highlight the uniformity allowed through our microwave-based intermetallic transformation, a comparison of the NCs using scanning transmission electron microscopy (STEM) after both microwave and thermal treatments is shown in Figure 2A–C.

Figure 2A–C shows $PtCo_2Cu_{0.19}$ NCs after ligand removal, after thermal treatment, and after microwave treatment, respectively. As apparent from the TEM micrographs, the thermal treatment causes significant NC aggregation, while the microwave treatment does not. To quantify NC sintering, we define the degree of aggregation as the increase in the standard deviation of diameter of the NCs with respect to the diamter of the NCs before deposition on carbon:

$$\text{aggregation}_{\text{sample}}(\%) = 100 \cdot \frac{\sqrt{\text{variance}(d_{\text{sample}})} - \text{variance}(d_{\text{before deposition}})}{\text{mean}(d_{\text{before deposition}})}$$

By analyzing the TEM micrographs, we conclude that the aggregation in the A1 and MW-$L1_0$ samples amounts to 11.5 ± 1.6% and 12.5 ± 1.8%, respectively. This indicates that the microwave heating-induced phase transformation leads to no statistically significant increase in aggregation. HAADF-STEM tomography shown in the Supporting Information further confirms the lack of aggregation in the MW-$L1_0$ NCs. The thermally annealed NCs, however, show a significant increase in aggregation to 41.6 ± 7.2%. Overall, thermal and microwave treatments result in NC diameters of 9.4 ± 3.9 nm and 7.0 ± 1.0 nm, respectively. As shown in Figures S4–S6, the aggregation of the MW-$L1_0$ NCs will be affected by power level, treatment

https://doi.org/10.1021/acsmaterialslett.2c00174
ACS Materials Lett. 2022, 4, 823–830

time, and copper doping level, and therefore it is imperative to optimize these three amounts. As described in detail in section S3, we find that the minimum parameters needed to induce a phase transformation in the $PtCo_2$ MW-$L1_0$ NCs are 1200 W and 30 s; these parameters are used for the demonstrations reported here. Using lower power levels or treatment times does not result in phase transformations, as shown by $S^2 = 0$. We note that, while harmful to the ORR activity,[24] copper doping plays a key role in lowering the energy barrier for phase transformation due to melting point depression:[9,20,23,48] in the absence of doping, no intermetallic conversion was observed ($S^2 = 0$).

We now evaluate the electrocatalytic performance of both the A1 and $L1_0$ phases. The electrochemical stability data and ORR activity is shown in Figure 3A−F. The electrochemical testing methods used here follow standard practices.[13,49−52] To test for stability, the samples were cycled between 0.6 and 1.0 V vs RHE in N_2 saturated 0.1 M $HClO_4$, with Cyclic Voltammetry (CV) curves taken after 50 cycles at the beginning-of-life (BOL), 5000, and 25 000 cycles, shown in Figure 3A−C for the A1, Therm-$L1_0$, and MW-$L1_0$ samples, respectively. The ECSA was determined from the CV curves shown in Figure 3A−C using hydrogen underpotential deposition measurements.[52] The decrease in ECSA corresponds to a decrease in peak area as quantified in Table S2. Figure 3D shows that the BOL values of ECSA for the A1 phase and MW-$L1_0$ phase samples are statistically consistent at 100.9 ± 5.2 m^2/g and 106.2 ± 4.3 m^2/g, respectively, as expected from the absence of sintering during phase transformation for MW-$L1_0$ samples. In contrast, a decrease in BOL ECSA is observed for the Therm-$L1_0$ sample, at 87.0 ± 7.5 m^2/g. We attribute this decrease in ECSA of ∼14% to NC aggregation caused by thermal-annealing, consistent with the aggregation data presented in Figure 2D. This confirms that the thermal annealing method of phase transformation causes undesirable sintering while the MW-$L1_0$ sample shows no sintering. After electrochemical cycling, the ECSA of the A1 sample decreases to 70.8 ± 11.2 m^2/g, while the Therm-$L1_0$ and MW-$L1_0$ samples decrease to 79.2 ± 2.7 m^2/g and 92.0 ± 8.3 m^2/g, respectively, further confirming the superiority of microwave-annealing over thermal-annealing. This demonstrates ECSA retention of $70.1 \pm 5.8\%$, $90.0 \pm 3.6\%$, and $86.6 \pm 4.1\%$ for A1, Therm-$L1_0$, and MW-$L1_0$ NCs, respectively. Figure 3E shows representative ORR polarization curves illustrating a similar observed current density for all samples at 0.9 V vs RHE.[13] We note that the current density at potentials below 0.9 V vs RHE for the MW-$L1_0$ samples increases compared to the other samples, likely because of a decreased overpotential for ORR. As seen in Figure 3F, the mass activity per unit platinum is 163.7 ± 5.8 mA/mg, 260.1 ± 6.4 mA/mg, and 336.0 ± 4.6 mA/mg for Al, Therm-$L1_0$, and MW-$L1_0$ NCs, respectively. The microwave treated samples show an increased activity per unit mass Pt over the thermally transformed NCs of 22.6% and over the A1 samples of 51.3%. Instead, the activity per Pt active site, or specific activity, is approximately the same for the three samples. This indicates that the choice of NC treatment does not affect the activity per Pt active site; instead, the monodispersity of the NCs obtained through the microwave-based heating method allows for a greater mass activity for ORR. Importantly, the MW-$L1_0$ samples outperform the commercial standard for ORR, Pt/C NCs, in mass activity by 68.5%, as seen in section S6.

In conclusion, we demonstrate a rapid, 30 s microwave treatment to drive the phase transformation of Cu-doped Pt−Co alloy NCs into the intermetallic $L1_0$ phase while minimizing colloidal aggregation and sintering. We confirm the completeness of the phase transformation from the random alloy A1 phase into the intermetallic $L1_0$ phase by using HAADF-STEM imaging, XRD, and SQUID magnetometry. To ensure a quantitative comparison, we monitored morphological changes in NCs undergoing either microwave or thermal treatment. We show that while the aggregation for thermally annealed NCs increases by nearly 30%, the microwave-treated NCs do not show any statistically significant evidence of aggregation. Importantly, while both microwave-treated and thermally annealed NC samples display electrochemical stability of approximately 90% after 25 000 cycles, the microwave-treated NCs show a mass activity ∼30% higher than the thermally annealed samples. We anticipate this rapid and efficient method to trigger intermetallic phase transformations to be readily applicable to other NC systems and particularly beneficial to systems where maintaining the NC monodispersity is crucial to catalytic performance.[1,7,11,26,45]

EXPERIMENTAL METHODS

Platinum(II) acetylacetonate ($Pt(acac)_2$, 98%), dicobalt octacarbonyl ($Co_2(CO)_8$, 95%), 1,2-dichlorobenzene (DCB, 99%), 1-octadecene (ODE, 90%), and 1-adamantane carboxylic acid (ADCA, 99%) were purchased from Acros Organics. Oleylamine (OLAM, 70%), Nafion (5% in a mixture of 2-propanol and water), and copper(II) acetylacetonate ($Cu(acac)_2$, 97%), were purchased from Sigma-Aldrich.

NCs were synthesized via a modified solvothermal method previously reported by Lee et al.,[13] and Luo et al.[45] For the synthesis of the NCs used in this report, $Pt(acac)_2$ (0.67 mmol), ADCA (3.7 mmol), and the desired amount of $Cu(acac)_2$ dopant (here 5% the Pt amount) were dissolved in OLAM (41 mL) and ODE (16 mL). The reaction was purged at 80 °C for 30 min under a 0.100 Torr vacuum. The reaction was then heated to 300 °C in an N_2 atmosphere at 10 °C/min. During the temperature rise, $Co_2(CO)_8$ (0.3 mmol in 3.2 mL DCB) was rapidly injected at 170 °C. After 30 min at a high temperature, the reaction was cooled to room temperature, and the resulting NCs were purified by precipitation with ethanol and centrifugation at 6000 rpm for 6 min and resuspended in hexanes. Note: the use of ultrahigh purity (200 proof) ethanol is needed to precipitate the NCs without colloidal phase segregation. The stoichiometry of the NCs can be adjusted following the same procedure with modification of the precursor ratios.

After purification, the hexane dispersed NCs were mixed with Vulvan XC-72 carbon powder at 20.0 wt % metal loading. The solution was sonicated for 1 h and centrifuged at 8000 rpm for 3 min or until precipitated. The supernatant was discarded, and the precipitate was washed twice with acetone and subsequently centrifuged. The samples were dried overnight under vacuum at 50 °C. To remove the organic ligands, the samples were treated in a precleaned Harrick Plasma O_2 plasma cleaner for 15 min and then were transferred for 1 min in a preheated 500 °C muffle furnace.

For thermally transformed NCs, the carbon-supported samples were placed in a tube furnace under a 5% H_2 environment, balanced with N_2. These NCs were treated for 4 h at 650 °C, as described in previous reports,[13] to obtain intermetallic $L1_0$ phase NCs. For microwave transformed NCs, 15 mg of carbon-supported samples was placed in the microwave hot-spot, in a sealed quartz vessel under 5% H_2 balanced with N_2. The samples were treated at 1200 W for 30 s

https://doi.org/10.1021/acsmaterialslett.2c00174
ACS Materials Lett. 2022, 4, 823−830

to obtain intermetallic NCs. More information on the microwave-based conversion is in section S2.

TEM micrographs were collected on either a JEOL JEM-1400 microscope operating at 120 keV or a JEOL JEM-F200 multipurpose electron microscope operating at 200 keV. High-resolution HAADF-STEM and EDS were collected on a JEOL NEOARM operating at 200 kV. The probe current was 150 pA, and the camera length was 4 cm. STEM simulations were performed using ReciPro.[53] EDS maps were obtained with Digital Micrograph, software provided by Gatan Inc. Elemental composition was determined using inductively coupled plasma-optical emission spectrometry (ICP-OES) performed on a Spectro Genesis spectrometer with a concentric nebulizer. XRD patterns were collected in the 2θ range of 20°−90°, with data points collected every 0.02°2θ, and a scan rate of 0.15°/s on a Rigaku Smartlab high-resolution diffractometer with Cu Kα radiation (λ = 0.154 16 nm, 44 mA, and 30 kV). DC magnetometry was performed on a SQUID magnetometer from quantum design. Hysteresis was measured at 300 K from −3.0 to +3.0 T.

Electrochemical measurements were performed using standard protocols.[49−51] Data were collected on a potentiostat (Epsilon, Bioanalytical Systems Inc.) with a three-electrode system consisting of a glassy carbon working electrode (6 mm diameter), an Ag/AgCl reference electrode in 3 M KCl, and a Pt Coil auxiliary electrode. All potentials collected during the testing were converted in reference to a reversible hydrogen electrode (RHE). The catalyst ink was formed through sonication of water, isopropyl alcohol, and Nafion at a volume ratio of 4 to 1 to 0.01 and an NC on carbon concentration of 2.0 mg/mL. Then 10.0 μL of ink was deposited onto the working electrode and dried under rotation. CV was taken in a range of 0.000 to 1.000 V vs RHE at a scan rate of 50.000 mV/s in N_2 saturated 0.1 M $HClO_4$. Linear sweep voltammetry was conducted in an O_2 saturated 0.1 M $HClO_4$ solution to determine the ORR activity between 0.100 and 1.100 V vs RHE at 10.0 mV/s and a rotation rate of 1600 rpm.

■ ASSOCIATED CONTENT

Supporting Information

The Supporting Information is available free of charge at https://pubs.acs.org/doi/10.1021/acsmaterialslett.2c00174.

Additional method details; microwave hotspot determination; additional overview of experimental parameters; XRD simulation details; additional microscopy; Comm-Pt electrochemical plots; HAADF-STEM tomography for MW-$L1_0$ and Therm-$L1_0$ (PDF)

Movie S1 showing Therm-$L1_0$ transformation (MP4)

Movie S2 showing MW-$L1_0$ transformation (MP4)

■ AUTHOR INFORMATION

Corresponding Author

Christopher B. Murray − *Department of Materials Science and Engineering and Department of Chemistry, University of Pennsylvania, Philadelphia, Pennsylvania 19104, United States*; Email: cbmurray@sas.upenn.edu

Authors

Daniel J. Rosen − *Department of Materials Science and Engineering, University of Pennsylvania, Philadelphia, Pennsylvania 19104, United States*; orcid.org/0000-0003-1463-7363

Alexandre C. Foucher − *Department of Materials Science and Engineering, University of Pennsylvania, Philadelphia, Pennsylvania 19104, United States*; orcid.org/0000-0001-5042-4002

Jennifer D. Lee − *Department of Chemistry, University of Pennsylvania, Philadelphia, Pennsylvania 19104, United States*; orcid.org/0000-0003-2644-3507

Shengsong Yang − *Department of Chemistry, University of Pennsylvania, Philadelphia, Pennsylvania 19104, United States*; orcid.org/0000-0002-1386-7549

Emanuele Marino − *Department of Chemistry, University of Pennsylvania, Philadelphia, Pennsylvania 19104, United States*; orcid.org/0000-0002-0793-9796

Eric A. Stach − *Department of Materials Science and Engineering, University of Pennsylvania, Philadelphia, Pennsylvania 19104, United States*; orcid.org/0000-0002-3366-2153

Complete contact information is available at: https://pubs.acs.org/10.1021/acsmaterialslett.2c00174

Author Contributions

D.J.R. performed the synthesis, and transformation of the nanocrystals. A.C.F. performed atomic-resolution STEM imaging. E.A.S. oversaw the atomic-resolution STEM imaging. J.D.L. performed ICP and assisted with the work. D.J.R. performed catalytic testing. S.Y. assisted with catalytic testing. D.J.R. and S.Y. performed tomography. D.J.R. and E.M. performed thermal calculations. C.B.M. oversaw the work. D.J.R. wrote the first draft of the paper. The paper was revised through contributions by all authors.

Notes

The authors declare no competing financial interest.

■ ACKNOWLEDGMENTS

D.J.R., J.D.L., S.Y., and C.B.M. acknowledge primary support from the Catalysis Center for Energy Innovation, an Energy Frontier Research Center funded by the U.S. Department of Energy, Office of Science, Office of Basic Energy Sciences under Award No. DE-SC0001004. E.M. and C.B.M. acknowledge support from the Office of Naval Research Multidisciplinary University Research Initiative Award ONR N00014-18-1-2497. A.C.F and E.A.S acknowledge support from Integrated Mesoscale Architectures for Sustainable Catalysis (IMASC), an Energy Frontier Research Center funded by the U.S. Department of Energy, Office of Science, Basic Energy Sciences under Award #DE-SC0012573. D.J.R. and A.C.F. acknowledge support from the Vagelos Institute for Energy Science and Technology Fellowship Program. C.B.M. acknowledges the Richard Perry University Professorship at the University of Pennsylvania. This work was carried out in part at the Singh Center for Nanotechnology, which is supported by the NSF National Nanotechnology Coordinated Infrastructure Program under grant NNCI-2025608. Additional support to the Nanoscale Characterization Facility at the Singh Center has been provided by the Laboratory for Research on the Structure of Matter (MRSEC) supported by the National Science Foundation (DMR-1720530).

■ REFERENCES

(1) Kim, H. Y.; Joo, S. H. Recent Advances in Nanostructured Intermetallic Electrocatalysts for Renewable Energy Conversion Reactions. *Journal of Materials Chemistry A* **2020**, *8*, 8195−8217.

(2) Xiao, W.; Lei, W.; Gong, M.; Xin, H. L.; Wang, D. Recent Advances of Structurally Ordered Intermetallic Nanoparticles for Electrocatalysis. *ACS Catal.* **2018**, *8*, 3237−3256.
(3) Yuan, Y.; Yang, Z.; Lai, W.; Gao, L.; Li, M.; Zhang, J.; Huang, H. Intermetallic Compounds: Liquid-Phase Synthesis and Electrocatalytic Applications. *Chem.—Eur. J.* **2021**, *27*, 16564−16580.
(4) Sun, H.; Song, S.; Xu, X.; Dai, J.; Yu, J.; Zhou, W.; Shao, Z.; Jung, W. C. Recent Progress on Structurally Ordered Materials for Electrocatalysis. *Adv. Energy Mater.* **2021**, *11*, 2101937.
(5) Flores Espinosa, M. M.; Cheng, T.; Xu, M.; Abatemarco, L.; Choi, C.; Pan, X.; Goddard, W. A.; Zhao, Z.; Huang, Y. Compressed Intermetallic PdCu for Enhanced Electrocatalysis. *ACS Energy Letters* **2020**, *5*, 3672−3680.
(6) Zhou, M.; Li, C.; Fang, J. Noble-Metal Based Random Alloy and Intermetallic Nanocrystals: Syntheses and Applications. *Chem. Rev.* **2021**, *121*, 736−795.
(7) Wang, D.; Xin, H. L.; Hovden, R.; Wang, H.; Yu, Y.; Muller, D. A.; Disalvo, F. J.; Abruña, H. D. Structurally Ordered Intermetallic Platinum-Cobalt Core-Shell Nanoparticles with Enhanced Activity and Stability as Oxygen Reduction Electrocatalysts. *Nature Materials 2012 12:1* **2013**, *12*, 81−87.
(8) Bueno, S. L. A.; Ashberry, H. M.; Shafei, I.; Skrabalak, S. E. Building Durable Multimetallic Electrocatalysts from Intermetallic Seeds. *Acc. Chem. Res.* **2021**, *54*, 1662−1672.
(9) Shen, R.; Wu, X.; Li, X.; Huang, J.; Luo, S.; Li, J.; Qian, N.; Ji, L.; Yang, D.; Zhang, H. Ga-Doped Intermetallic Pd_3Pb Nanocubes as a Highly Efficient and Durable Oxygen Reduction Reaction Electrocatalyst. *ChemistrySelect* **2021**, *6*, 3891−3896.
(10) Tetteh, E. B.; Lee, H.-Y.; Shin, C.-H.; Kim, S.; Ham, H. C.; Tran, T.-N.; Jang, J.-H.; Yoo, S. J.; Yu, J.-S. New PtMg Alloy with Durable Electrocatalytic Performance for Oxygen Reduction Reaction in Proton Exchange Membrane Fuel Cell. *ACS Energy Letters* **2020**, *5*, 1601−1609.
(11) Lin, R.; Zheng, T.; Chen, L.; Wang, H.; Cai, X.; Sun, Y.; Hao, Z. Anchored Pt-Co Nanoparticles on Honeycombed Graphene as Highly Durable Catalysts for the Oxygen Reduction Reaction. *ACS Appl. Mater. Interfaces* **2021**, *13*, 34397−34409.
(12) Xiong, Y.; Yang, Y.; DiSalvo, F. J.; Abruna, H. D. Synergistic Bimetallic Metallic Organic Framework-Derived Pt-Co Oxygen Reduction Electrocatalysts. *ACS Nano* **2020**, *14*, 13069−13080.
(13) Lee, J. D.; Jishkariani, D.; Zhao, Y.; Najmr, S.; Rosen, D.; Kikkawa, J. M.; Stach, E. A.; Murray, C. B. Tuning the Electrocatalytic Oxygen Reduction Reaction Activity of Pt-Co Nanocrystals by Cobalt Concentration with Atomic-Scale Understanding. *ACS Appl. Mater. Interfaces* **2019**, *11*, 26789−26797.
(14) Gao, P.; Pu, M.; Chen, Q.; Zhu, H. Pt-Based Intermetallic Nanocrystals in Cathode Catalysts for Proton Exchange Membrane Fuel Cells: From Precise Synthesis to Oxygen Reduction Reaction Strategy. *Catalysts* **2021**, *11*, 1050.
(15) Wang, S.; Xu, W.; Zhu, Y.; Luo, Q.; Zhang, C.; Tang, S.; Du, Y. Synthesis of Structurally Stable and Highly Active $PtCo_3$ Ordered Nanoparticles through an Easily Operated Strategy for Enhanced Oxygen Reduction Reaction. *ACS Appl. Mater. Interfaces* **2021**, *13*, 827−835.
(16) Yu, Y.; He, L.; Xu, J.; Li, J.; Jiang, S.; Han, G.; Jiang, B.; Lei, W.; Yang, W.; Hou, Y. A Facile Solution Phase Synthesis of Directly Ordering Monodisperse FePt Nanoparticles. *Nano Research 2021 15:1* **2022**, *15*, 446−451.
(17) Yu, Y.; Mukherjee, P.; Tian, Y.; Li, X. Z.; Shield, J. E.; Sellmyer, D. J. Direct Chemical Synthesis of $L1_0$-FePtAu Nanoparticles with High Coercivity. *Nanoscale* **2014**, *6*, 12050−12055.
(18) Li, Q.; Wu, L.; Wu, G.; Su, D.; Lv, H.; Zhang, S.; Zhu, W.; Casimir, A.; Zhu, H.; Mendoza-Garcia, A.; Sun, S. New Approach to Fully Ordered Fct-FePt Nanoparticles for Much Enhanced Electrocatalysis in Acid. *Nano Lett.* **2015**, *15*, 2468−2473.
(19) Liu, M.; Xiao, X.; Li, Q.; Luo, L.; Ding, M.; Zhang, B.; Li, Y.; Zou, J.; Jiang, B. Recent Progress of Electrocatalysts for Oxygen Reduction in Fuel Cells. *J. Colloid Interface Sci.* **2022**, *607*, 791−815.
(20) Yang, C. L.; Wang, L. N.; Yin, P.; Liu, J.; Chen, M. X.; Yan, Q. Q.; Wang, Z. S.; Xu, S. L.; Chu, S. Q.; Cui, C.; Ju, H.; Zhu, J.; Lin, Y.; Shui, J.; Liang, H. W. Sulfur-Anchoring Synthesis of Platinum Intermetallic Nanoparticle Catalysts for Fuel Cells. *Science* **2021**, *374*, 459−464.
(21) Yang, Y.; Wang, Z.; Mai, Y.; Guo, C.; Shi, Y.; Tan, H.; Lu, Z.; Shen, L.; Yan, C. Highly Active PtCo Nanoparticles on Hierarchically Ordered Mesoporous Carbon Support for Polymer Electrolyte Membrane Fuel Cells. *Journal of Materials Science 2021 56:23* **2021**, *56*, 13083−13095.
(22) Whiston, M. M.; Azevedo, I. L.; Litster, S.; Whitefoot, K. S.; Samaras, C.; Whitacre, J. F. Expert Assessments of the Cost and Expected Future Performance of Proton Exchange Membrane Fuel Cells for Vehicles. *Proc. Natl. Acad. Sci. U.S.A.* **2019**, *116*, 4899−4904.
(23) Liu, Y.; Wang, Y.; Yang, P.; Gao, G. Composition Adjustment of PtCoCu Alloy Assemblies towards Improved Hydrogen Evolution and Methanol Oxidation Reaction. *Int. J. Hydrogen Energy* **2021**, *46*, 37311−37320.
(24) Yin, S.; Shen, Y.; Zhang, J.; Yin, H. M.; Liu, X. Z.; Ding, Y. Tuning the Electronic Structure of Nanoporous Ag via Alloying Effect from Cu to Boost the ORR and Zn-Air Battery Performance. *Appl. Surf. Sci.* **2021**, *545*, 149042.
(25) Li, J.; Sharma, S.; Wei, K.; Chen, Z.; Morris, D.; Lin, H.; Zeng, C.; Chi, M.; Yin, Z.; Muzzio, M.; Shen, M.; Zhang, P.; Peterson, A. A.; Sun, S. Anisotropic Strain Tuning of $L1_0$ ternary Nanoparticles for Oxygen Reduction. *J. Am. Chem. Soc.* **2020**, *142*, 19209−19216.
(26) Jayasayee, K.; van Veen, J. A. R.; Manivasagam, T. G.; Celebi, S.; Hensen, E. J. M.; de Bruijn, F. A. Oxygen Reduction Reaction (ORR) Activity and Durability of Carbon Supported PtM (Co, Ni, Cu) Alloys: Influence of Particle Size and Non-Noble Metals. *Appl. Catal. B: Environ.* **2012**, *111−112*, 515−526.
(27) Ashberry, H. M.; Zhan, X.; Skrabalak, S. E. Identification of Nanoscale Processes Associated with the Disorder-to-Order Transformation of Carbon-Supported Alloy Nanoparticles. *ACS Materials Au* **2022**, *2*, 143−153.
(28) Shih, K. Y.; Wei, J. J.; Tsai, M. C. One-Step Microwave-Assisted Synthesis of PtNiCo/RGO Electrocatalysts with High Electrochemical Performance for Direct Methanol Fuel Cells. *Nanomaterials 2021, Vol. 11, Page 2206* **2021**, *11*, 2206.
(29) Teichert, J.; Heise, M.; Chang, J. H.; Ruck, M. Refinement of the Microwave-Assisted Polyol Process for the Low-Temperature Synthesis of Intermetallic Nanoparticles. *Eur. J. Inorg. Chem.* **2017**, *2017*, 4930−4938.
(30) Wang, Y.; Hall, A. S. Room-Temperature Synthesis of Intermetallic Cu-Zn by an Electrochemically Induced Phase Transformation. *Chem. Mater.* **2021**, *33*, 7309−7314.
(31) Loc Nguyen, H.; Howard, L. E. M.; Giblin, S. R.; Tanner, B. K.; Terry, I.; Hughes, A. K.; Ross, I. M.; Serres, A.; Bürckstümmer, H.; Evans, J. S. O. Synthesis of Monodispersed Fcc and Fct FePt/FePd Nanoparticles by Microwave Irradiation. *J. Mater. Chem.* **2005**, *15*, 5136−5143.
(32) Wang, Y.; Sun, D.; Chowdhury, T.; Wagner, J. S.; Kempa, T. J.; Hall, A. S. Rapid Room Temperature Synthesis of a Metastable Ordered Intermetallic Electrocatalyst. *J. Am. Chem. Soc.* **2019**, *141*, 2342−2347.
(33) Song, P.; Lei, Y.; Hu, X.; Wang, C.; Wang, J.; Tang, Y. Rapid One-Step Synthesis of Carbon-Supported Platinum-Copper Nanoparticles with Enhanced Electrocatalytic Activity via Microwave-Assisted Heating. *J. Colloid Interface Sci.* **2020**, *574*, 421−429.
(34) Wang, Y.; Gong, T.; Lee, M.; Hall, A. S. Structural Transformations of Metal Alloys under Electrocatalytic Conditions. *Current Opinion in Electrochemistry* **2021**, *30*, 100796.
(35) Gunji, T.; Noh, S. H.; Ando, F.; Tanabe, T.; Han, B.; Ohsaka, T.; Matsumoto, F. Electrocatalytic Activity of Electrochemically Dealloyed $PdCu_3$ Intermetallic Compound towards Oxygen Reduction Reaction in Acidic Media. *Journal of Materials Chemistry A* **2018**, *6*, 14828−14837.
(36) Sun, D.; Wang, Y.; Livi, K. J. T.; Wang, C.; Luo, R.; Zhang, Z.; Alghamdi, H.; Li, C.; An, F.; Gaskey, B.; Mueller, T.; Hall, A. S. Ordered Intermetallic Pd_3Bi Prepared by an Electrochemically Induced Phase

Transformation for Oxygen Reduction Electrocatalysis. *ACS Nano* **2019**, *13*, 10818−10825.
(37) Fan, Z.; Cappelluti, M. D.; Gregory, D. H. Ultrafast, Energy-Efficient Synthesis of Intermetallics; Microwave-Induced Metal Plasma (MIMP) Synthesis of Mg_2Sn. *ACS Sustainable Chem. Eng.* **2019**, *7*, 19686−19698.
(38) Lekse, J. W.; Stagger, T. J.; Aitken, J. A. Microwave Metallurgy: Synthesis of Intermetallic Compounds via Microwave Irradiation. *Chem. Mater.* **2007**, *19*, 3601−3603.
(39) Du, C. K.; Zhou, S. C. Reaction Sintering of Mg_2Si Intermetallic Compound by Microwave Irradiation. *Advanced Materials Research* **2012**, *512*−*515*, 1683−1686.
(40) Xu, L.; Srinivasakannan, C.; Zhang, L.; Yan, M.; Peng, J.; Xia, H.; Guo, S. Fabrication of Tungsten-Copper Alloys by Microwave Hot Pressing Sintering. *J. Alloys Compd.* **2016**, *658*, 23−28.
(41) Li, H.; Zhang, C.; Pang, C.; Li, X.; Gao, X. The Advances in the Special Microwave Effects of the Heterogeneous Catalytic Reactions. *Frontiers in Chemistry* **2020**, *8*, 355.
(42) Muley, P. D.; Wang, Y.; Hu, J.; Shekhawat, D. Microwave-Assisted Heterogeneous Catalysis. *Catalysis* **2021**, *33*, 1−37.
(43) Ano, T.; Tsubaki, S.; Liu, A.; Matsuhisa, M.; Fujii, S.; Motokura, K.; Chun, W. J.; Wada, Y. Probing the Temperature of Supported Platinum Nanoparticles under Microwave Irradiation by in Situ and Operando XAFS. *Communications Chemistry 2020 3:1* **2020**, *3*, 1−11.
(44) Rosen, D. J.; Yang, S.; Marino, E.; Jiang, Z.; Murray, C. B. In Situ EXAFS-Based Nanothermometry of Heterodimer Nanocrystals under Induction Heating. *J. Phys. Chem. C* **2022**, *126*, 3623−3634.
(45) Luo, J.; Yun, H.; Mironenko, A. v.; Goulas, K.; Lee, J. D.; Monai, M.; Wang, C.; Vorotnikov, V.; Murray, C. B.; Vlachos, D. G.; Fornasiero, P.; Gorte, R. J. Mechanisms for High Selectivity in the Hydrodeoxygenation of 5-Hydroxymethylfurfural over PtCo Nanocrystals. *ACS Catal.* **2016**, *6*, 4095−4104.
(46) Foucher, A. C.; Marcella, N.; Lee, J. D.; Rosen, D. J.; Tappero, R.; Murray, C. B.; Frenkel, A. I.; Stach, E. A. Structural and Valence State Modification of Cobalt in CoPt Nanocatalysts in Redox Conditions. *ACS Nano* **2021**, *15*, 20619−20632.
(47) Gordon, T. R.; Diroll, B. T.; Paik, T.; Doan-Nguyen, V. V. T.; Gaulding, E. A.; Murray, C. B. Characterization of Shape and Monodispersity of Anisotropic Nanocrystals through Atomistic X-Ray Scattering Simulation. *Chem. Mater.* **2015**, *27*, 2502−2506.
(48) Hock, C.; Straßburg, S.; Haberland, H.; Issendorff, B. v.; Aguado, A.; Schmidt, M. Melting-Point Depression by Insoluble Impurities: A Finite Size Effect. *Phys. Rev. Lett.* **2008**, *101*, 023401.
(49) Schmidt, T. J.; Gasteiger, H. A.; Stäb, G. D.; Urban, P. M.; Kolb, D. M.; Behm, R. J. Characterization of High-Surface-Area Electrocatalysts Using a Rotating Disk Electrode Configuration. *J. Electrochem. Soc.* **1998**, *145*, 2354−2358.
(50) Xia, Y.-F.; Guo, P.; Li, J.-Z.; Zhao, L.; Sui, X.-L.; Wang, Y.; Wang, Z.-B. How to Appropriately Assess the Oxygen Reduction Reaction Activity of Platinum Group Metal Catalysts with Rotating Disk Electrode. *iScience* **2021**, *24*, 103024.
(51) Bird, M. A.; Goodwin, S. E.; Walsh, D. A. Best Practice for Evaluating Electrocatalysts for Hydrogen Economy. *ACS Appl. Mater. Interfaces* **2020**, *12*, 20500−20506.
(52) Mayrhofer, K. J. J.; Strmcnik, D.; Blizanac, B. B.; Stamenkovic, V.; Arenz, M.; Markovic, N. M. Measurement of Oxygen Reduction Activities via the Rotating Disc Electrode Method: From Pt Model Surfaces to Carbon-Supported High Surface Area Catalysts. *Electrochim. Acta* **2008**, *53*, 3181−3188.
(53) Seto, Y.; Ohtsuka, M. ReciPro: Free and Open-Source Multipurpose Crystallographic Software Integrating a Crystal Model Database and Viewer, Diffraction and Microscopy Simulators, and Diffraction Analysis Tools. *J. Appl. Crystallogr.* **2022**, *55*. DOI: 10.1107/S1600576722000139.

https://doi.org/10.1021/acsmaterialslett.2c00174
ACS Materials Lett. 2022, 4, 823−830